nanomaterials

MDPI

Article

Multiferroic, Phonon and Optical Properties of Pure and Ion-Doped YFeO₃ Nanoparticles

Angel Apostolov [1], Iliana Apostolova [2] and Julia Wesselinowa [3,*]

[1] Civil Engineering and Geodesy, Hristo Smirnenski Blvd. 1, University of Architecture, 1046 Sofia, Bulgaria; angelapos@abv.bg
[2] Kl. Ohridsky Blvd. 10, University of Forestry, 1756 Sofia, Bulgaria; inaapos@abv.bg
[3] J. Bouchier Blvd. 5, Sofia University "St. Kliment Ohridski", 1164 Sofia, Bulgaria
[*] Correspondence: julia@phys.uni-sofia.bg

Abstract: The magnetic, electric, phonon and optical properties of pure and ion-doped orthorhombic YFeO₃ nanoparticles are studied for the first time theoretically. The spontaneous magnetization M_s in YFeO₃ decreases with decreasing particle size. M_s is also shape dependent. The magnetization increases by Co and Er ion doping and decreases by Ti doping, which is caused by the different strain which appears in the nanoparticles and changes the exchange interaction constants in the doped states. The phonon energy for the A_g mode $\omega = 149$ cm^{-1} and their damping decreases or increases with increasing temperature, respectively. Both show a kink near the Neel temperature, T_N, which disappears by applying an external magnetic field. The influence of different ion doping on the band gap energy is also discussed. The doping effects can be used for different applications.

Keywords: ion-doped YFeO₃ nanoparticles; magnetization; polarization; phonon energy; band gap; microscopic model

1. Introduction

Yttrium orthoferrite YFeO₃ (YFO) is of interest due to its significant physical properties connected with different micro-technological devices [1–5]. YFO is an antiferromagnet with a super-exchange magnetic interaction between two Fe³⁺ ions, the arrangement of which is not perfectly antiparallel, leading to a weak ferromagnetism with a Neel temperature of $T_N \sim 640$ K [1,2]. Moreover, a saturation polarization at room temperature is observed [2,5–7], which is an evidence for the multiferroism of YFO. YFO is a type II multiferroic. The microscopic origin of the ferroelectric polarization is considered a spin-exchange striction [7]. The Raman spectra of YFO have been investigated by Raut et al. [8], Saha et al. [9] and Coutinho et al. [10]. Raut et al. [8] have reported an anomalous phonon behaviour near T_N.

The doping of YFO with different ions—magnetic or nonmagnetic—can improve its magnetic, electric and dielectric properties. Many authors have studied the changes in the properties of YFO which occur though the substitution of different ions on Y-, Fe- or both sites in YFO bulk and nanoparticles [11–26]. The doping ions have different ionic radii in comparison with the host ions, which leads to strains and to modification of the properties after ion doping. Let us emphasize that there are some discrepancies in the reported results, for example, by Ti ion doping; see Refs. [14–16]. We will try to clarify them.

There are not so many theoretical papers which have investigated the multiferroic, phonon and optical properties of doped YFO, either in bulk and nanoparticles. Usually, the magnetic properties of the undoped bulk compounds are considered. The magnetic interactions in RFeO₃, with R = yttrium or a rare earth, have been reported already by Treves [27]. In order to explain the low-energy magnetic excitations of YFO and LaFeO₃, Park et al. [28] have used a spin Hamiltonian taking into account the Dzyaloshinsky–Moriya interaction (DMI). The electronic structure and the magnetic properties of the YFO

perovskite have been studied by Stoeffler and Chaker [29] using the density-functional theory with the so-called Hubbard correction. Using a first-principles study, the structural, ferroelectric and optical properties of pure and Bi-doped YFO were analyzed recently by Martinez-Aguilar et al. [30].

In the present work, using a microscopic model and the Green's function technique, we will investigate the size and ion doping effects on the multiferroic, phonon and optical properties of orthorhombic YFO bulk and nanoparticles.

2. Model and Methods

The multiferroic properties of YFO are described by the following Hamiltonian:

$$H = H_m + H_e + H_{me}. \tag{1}$$

The first term in Equation (1) is a modified Heisenberg's Hamiltonian for the magnetic behavior:

$$
\begin{aligned}
H_m &= -\sum_{ij}(1-x)J_{ij}^{Fe-Fe}\mathbf{S}_i^{Fe} \cdot \mathbf{S}_j^{Fe} - \sum_{ij}xJ_{ij}^{Fe-DI}\mathbf{S}_i^{Fe} \cdot \mathbf{S}_j^{DI} \\
&\quad - \sum_{<ij>}J_{il}'^{Fe-Fe}\mathbf{S}_i^{Fe} \cdot \mathbf{S}_l^{Fe} - \sum_{ij}\mathbf{D}_{ij} \cdot [\mathbf{S}_i^{Fe} \times \mathbf{S}_j^{Fe}] - K\sum_i(S_i^{zFe})^2 \\
&\quad - g\mu_B\sum_i\mathbf{h} \cdot \mathbf{S}_i^{Fe},
\end{aligned}
\tag{2}
$$

where $\mathbf{S}_i$ is the Heisenberg spin operator of the Fe^{3+} ion, and J_{ij} and J_{il}' are the exchange interactions between the nearest neighbours and next-nearest neighbours. J^{Fe-DI} is the exchange interaction between the Fe and the doping ions (DI). $\mathbf{D}_{ij}$ represents the DMI vector. K is the single-ion anisotropy. $\mathbf{h}$ is an external magnetic field. x is the concentration of the doped ions at Fe states.

In Figure 1, a schematic presentation is given of the directions of the components of the Fe ions (open circle) and the position of the non-magnetic Y ions (full circle) in the magnetic phase. The spin structure in YFO has a net ferromagnetic moment in the z direction, $< S^z >$. The DMI, which is perpendicular to the easy axis, causes an additional canting of the antiferromagnetically ordered spins and creates weak magnetization. The magnetic field is applied in the z direction.
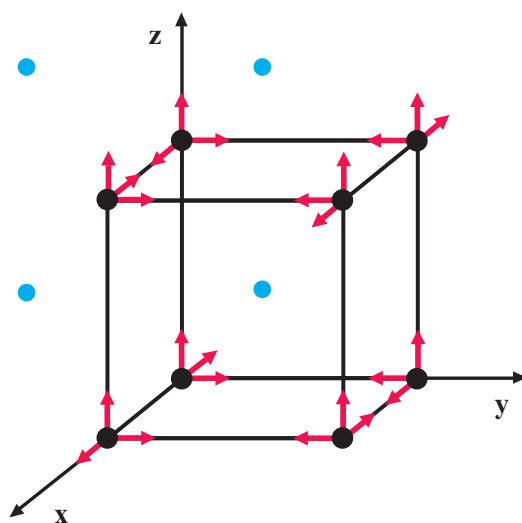

Figure 1. (Color online) Schematic presentation of the directions of the components of the Fe^{3+} spins (black circle) and the position of the non-magnetic Y ions (blue circle) in the magnetic phase.

From the spin Green's function $g_{ij}(E) = \langle\langle S_i^{Fe+}; S_j^{Fe-}\rangle\rangle$ the magnetization $M = \langle S^z\rangle$ for arbitrary spin value S is calculated as:

$$M(T) = \frac{1}{N}\sum_i \left[(S+0.5)\coth[(S+0.5)\beta E_{mi}] - 0.5\coth(0.5\beta E_{mi}) \right], \qquad (3)$$

where $\beta = 1/k_B T$, k_B is the Boltzmann constant and T is the absolute temperature. E_{mi} is the spin excitation energy. J is renormalized through the spin-phonon interactions F and R as well as the magnetoelectric coupling g to $J_{eff} = J_1 + 2F^2/(\omega_0 - MR) + 2gP^2\cos^2\theta$.

The spin-phonon interaction in YFO observed by Raut et al. [8] and Coutinho et al. [10] is taken into account in order to obtain correct results:

$$H_{sp-ph} = \frac{1}{2}\sum_{i,j,k} F(i,j,k)Q_i S_j^z S_k^z - \frac{1}{4}\sum_{i,j,r,s} R(i,j,r,s)Q_i Q_j S_r^z S_s^z + h.c. \qquad (4)$$

where F and R are the spin-phonon coupling constants in the first and second order.

The anharmonic phonon-phonon interactions are given by:

$$\begin{aligned} H_{ph} &= \frac{1}{2!}\sum_i \omega_{0i} a_i a_i^+ + \frac{1}{3!}\sum_{i,j,r} B(i,j,r)Q_i Q_j Q_r \\ &+ \frac{1}{4!}\sum_{i,j,r,s} A(i,j,r,s)Q_i Q_j Q_r Q_s, \end{aligned} \qquad (5)$$

where Q_i and ω_{0i} are the normal coordinate and frequency of the lattice mode.

From the phonon Green's function, defined via the phonon creation a^+ and annihilation a operators

$$G_{ij}(t) = \langle\langle a_i(t); a_j^+\rangle\rangle \qquad (6)$$

is observed the phonon energy ω and phonon damping γ

$$\gamma = \gamma_{sp-ph} + \gamma_{ph-ph} \qquad (7)$$

using the full Hamiltonian and the method of Tserkovnikov [31].

The Ising model in a transverse field describes the ferroelectric properties. It can be applied to order-disorder (KH_2PO_4) and displacive ($BaTiO_3$) type ferroelectrics [32,33]. The Hamiltonian reads:

$$H_e = \Omega\sum_i B_i^x - \frac{1}{2}\sum_{ij}(1-x')\tilde{J}_{ij} B_i^z B_j^z, \qquad (8)$$

where B_i^x, B_i^z are the spin-1/2 operators of the pseudo-spins, $\tilde{J}_{ij}$ denotes the pseudo-spin interaction, Ω is the tunneling frequency, and x' is the concentration of the doped ions at Y states.

The Y ion displacement and the FeO_6 octahedral distortion cause the spontaneous polarization [34,35], which is calculated to be:

$$\mathbf{P}_s = \left[\frac{1}{N'}\sum_i\langle B_i^x\rangle; 0; \frac{1}{N'}\sum_i\langle B_i^z\rangle \right]. \qquad (9)$$

H_{me} defines the magnetoelectric interaction between the two subsystems:

$$H_{me} = -\lambda\sum_{ij}(\mathbf{P}_s \times \mathbf{e}_{ij})\cdot(\mathbf{S}_i \times \mathbf{S}_j). \qquad (10)$$

where λ is the coupling constant and $\mathbf{e}_{ij}$ is the unit vector along the direction between the nearest-neighbours Fe^{3+}-ions.

The band gap energy E_g of YFO is defined by the difference between the valence and conduction bands:

$$E_g = \omega^+(\mathbf{k} = 0) - \omega^-(\mathbf{k} = \mathbf{k}_\sigma). \tag{11}$$

The electronic energies

$$\omega^\pm(k) = \epsilon_k - \frac{\sigma}{2}I\langle S^z\rangle \tag{12}$$

are observed from the Green's function $g(k,\sigma) = \ll c_{k,\sigma}; c_{k\sigma}^+ \gg$, $\sigma = \pm 1$, $c_{i\sigma}^+$ and $c_{i\sigma}$ are Fermi operators, and I is the s-d interaction constant [36].

3. Results and Discussion

A certain Fe-spin is fixed in the center of the nanoparticle with an icosahedral symmetry. All spins are included into shells numbered by $n = 1, ..., N$. $n = 1$ denotes the central spin and $n = N$ represents the surface shell [37].

The numerical calculations are made using the following model parameters: $J = -13.8$ cm^{-1}, $J' = -3.45$ cm^{-1}, $\tilde{J} = 575$ cm^{-1}, $\Omega = 21.4$ cm^{-1}, $D = 4.25$ cm^{-1}, $K = 0.09$ cm^{-1}, $\lambda = 1.4$ cm^{-1}, $T_N = 640$ K, $T_C = 420$ K [2,38], $F = 21$ cm^{-1}, $R = -18$ cm^{-1}, $B = -3$ cm^{-1}, and $A = 6.6$ cm^{-1}.

3.1. Size and Shape Dependence of the Magnetization

We will first demonstrate the size effects on the saturation magnetization M_s in a YFO nanoparticle. It must be noted that a weak magnetization in the case of antiferromagnetic nanoparticles can be due to uncompensated spins at the surface [39]. The exchange interaction constants on the surface, J_s, can be different than the bulk interaction constants, J_b, due to the reduced symmetry on the surface. We take for the numerical calculations the relation $J_s < J_b$. It must be noted that there is a competition between weak-ferromagnetic and antiferromagnetic interactions, which leads to the magnetic properties of a YFO nanoparticle. The results can be seen in Figure 2. The magnetization M_s decreases with decreasing nanoparticle size in concordance with the experimental data of Sui et al. [40] and Popkov et al. [41]. This reduction could be due to the existence of a spin-disordered surface layer, in which the thickness is larger than that of the lattice parameters in YFO. The investigations suggest a critical size of around $N_{cr} = 3$ shells, i.e., ~6 nm, below which there cannot exist a magnetic phase. Below N_{cr}, we have superparamagnetism. Let us emphasize that, by the numerical calculations, we can enhance the shells and for about N = 50 shells, i.e., about 100 nm (see Figure 2), in principle we reach the limit of the nanoparticle size which depends on the model parameters.
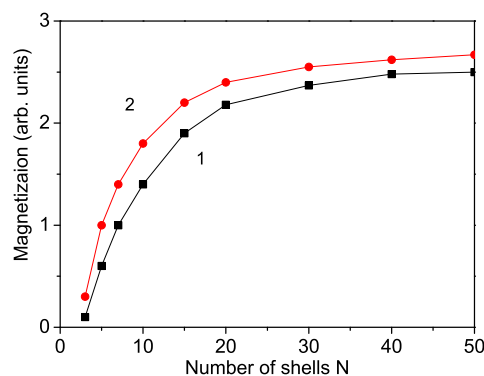

Figure 2. (Color online) The magnetization M_s as a function of size and shape in a YFO nanoparticle for $T = 300$ K, $J_s = 0.8J_b$, $h = 100$ Oe. (1) Spherical and (2) cylindrical.

The magnetic properties of YFO nanoparticles are shape dependent; see Figure 2, curve 2. The cylindrical nanoparticles show a higher saturation magnetization M_s than the spherical ones. A similar result has been observed by Yuan at al. [42]. A strong dimensional influence on the magnetic properties of YFO nanopowders was observed also by Popkov et al. [41].

3.2. Electric Field Dependence of the Polarization

In order to show the multiferroic properties of YFO, we have calculated the polarization of a YFO nanoparticle with $N = 10$ shells. The result is presented in Figure 3. The observed polarization loop provides evidence for the ferroelectric character and supports the multiferroism of YFO. A saturation polarization loop at room temperature in YFO nanoparticles is observed experimentally in Ref. [7]. It must be noted that the polarization decreases with decreasing nanoparticle size N (not shown here). There are not reported experimental data for $P(N)$.
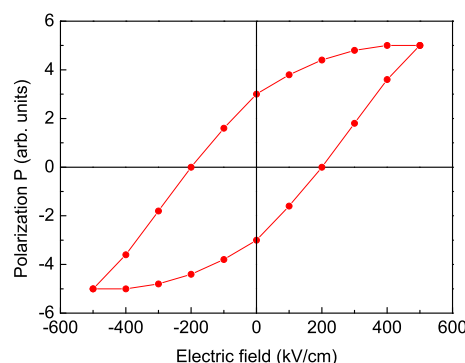

Figure 3. Electric field dependence of the spontaneous polarization P_s of a YFO nanoparticle for $T = 300$ K, $J'_s = 0.8J'_b$ and $N = 10$ shells.

3.3. Ion Doping Effects on the Magnetization

Let us emphasize that the concentration dependence of the magnetization is considered in the interval $0 \leq x \leq 0.3$, because in the most cases for larger x values a secondary phase is still presented.

3.3.1. Co Substitution at the Fe Site

The magnetic properties of ferrites can be improved through substitution of magnetic or nonmagnetic ions. As a next step, we will study the changes of the magnetic behaviour via doping of different ions at both sites, the Y-cation or Fe-cation site, in YFO nanoparticles. The doping ions substitute the host ions in a given shell, then in the next and so on, shell after shell. They are distributed in shells. By doping with the magnetic Co ion at the Fe site, $YFe_{1-x}Co_xO_3$, where the substitution of the Fe^{3+} ion ($r = 0.65$ Å) by the smaller Co^{3+} ion ($r = 0.55$ Å) leads to a lattice distortion and to a reduction of the unit cell parameters [12], i.e., to a compressive strain. In our model this means that the exchange interaction parameters between the Fe ions in the defect states J_d are larger compared to the undoped values J_b, $J_d > J_b$, because J is indirectly proportional to the distance between the spins. Moreover, by the calculations, the additive exchange interactions between the Co and the Co-Fe ions must be taken into account. Therefore, the saturation magnetization M_s increases with increasing values of the Co ion doping concentration x. This can also be explained by the increase of the magnetocrystalline anisotropy, because of the substitution of Co into the sites of Fe. Moreover, the Co^{2+} doping leads to modification of the Fe-O-Fe angles and to a small quantity of Fe^{4+} ions appearing to compensate the charge. The observed behavior is in good qualitative coincidence with the data of [12,24,43]. Our results are demonstrated in Figure 4, curve 1. By substituting a Fe ion with a larger Ni^{2+} ion, one study Nguyen et al. [44] has recently obtained a reduction of the lattice parameters, i.e., a compressive strain. In our model, we take the relation $J_d > J_b$ and observe again a larger magnetization M_s with rising Ni dopants. This is also shown in [44].
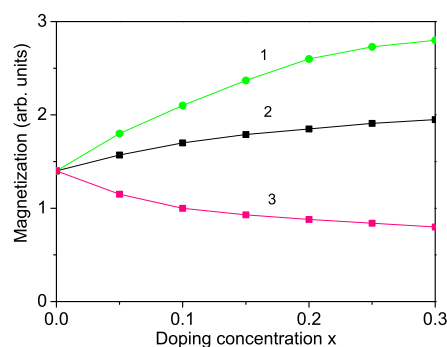
Figure 4. (Color online) The spontaneous magnetization M_s as a function of the doping concentration of a (1) Co-doped (with $J_d = 1.4J_b$), (2) Er-doped (with $J_d = 1.2J_b$) and (3) Ti-doped (with $J_d = 0.8J_b$) YFO nanoparticle for $T = 300$ K and $N = 10$ shells.

3.3.2. Er Substitution at the Y Site

By ion substituting at the Y site in YFO, it is possible to vary the magnetic properties. An increase in M_s is also obtained by a substitution of the Y ($r = 0.90$ Å) with the smaller Er ion ($r = 89$ Å), $Y_{1-x}Er_xFeO_3$. We have, again, a compressive strain which leads to an increase of J_d between the Fe ions, in comparison to the undoped case J_b, where $J_d > J_b$. The Fe-O-Fe superexchange interaction can affect the magnetization of Er-doped YFO [13]. This leads to an enhancing of M_s (see Figure 4, curve 2), which is in a good qualitative concordance with the results of Cheng et al. [11]. Let us emphasize that the observed saturation magnetization M_s is smaller than that in the case of Co ion doping at the Fe site. These enhanced magnetic properties could be of potential use for different applications.

3.3.3. Ca Substitution at the Y Site

We obtain also a small enhancement of the magnetization M_s with an increase in the doubly charged ion Ca^{2+} concentration in YFO at the Y site. The lattice parameters decrease slightly due to the different radii of the Ca ($r = 1.03$ Å) and Y ($r = 1.06$ Å) ions, which leads by using the relation $J_d > J_b$ to a higher magnetization in the doped YFO compared to the undoped one, in concordance with the results of Tien et al. [45]. The doping with Ca enhances the magnetocrystalline anisotropy of the $Y_{1-x}Ca_xFeO_3$ nanoparticles. Moreover, it requires a charge compensation, which can be reached by the transformation of a small part of ions from Fe^{3+} to Fe^{4+}, changing the Fe-O-Fe angles. With an increase in the Ca concentration, the charge compensating mechanism shifts from electron holes to oxygen vacancies.

3.3.4. Ti Substitution at the Fe Site

Let us emphasize that our model can also explain the experimentally observed reduction of the magnetization M_s and the Neel temperature T_N in Ti-doped YFO, $YFe_{1-x}Ti_xO_3$, nanoparticles [14,15]. This is due to the larger radius of the octahedral Ti^{4+} ion ($r = 0.745$ Å) relative to that of the host Fe^{3+} ion ($r = 0.69$ Å), which leads to a tensile strain. Moreover, a change in the valence states of Fe and Ti cations also explains the increase of the volume cell, which leads to the relation $J_d < J_b$. The result of the magnetization M_s as a function of the ion doping concentration x is presented in Figure 4, curve 3. Khalifa et al. [14] and Solorzano et al. [15] have reported that doping with Ti^{4+} ions lowers the Neel temperature T_N of YFO nanoparticles. Let us emphasize that our result does not agree with the reported improved magnetic properties of Ti-doped YFO ceramics by Madolappa et al. [16].

3.3.5. Mn Substitution at the Fe Site

We observe also a decrease of the magnetization M_s and the Neel temperature T_N by doping of YFO with the large anisotropic Mn ion at the Fe site of a $YFe_{1-x}Mn_xO_3$ nanoparticle, which is due to the weakening of the superexchange interaction after the Mn^{3+} substitution. Moreover, there appears to be a spin re-orientation transition and a

significant magnetic anisotropy by Mn doping. A similar decrease in the Neel temperature T_N and the spontaneous magnetization M_s with increasing Mn dopant concentration is observed experimentally by Deka et al. [46,47] and Sundarayya et al. [19].

3.4. Ion Doping Effects on the Polarization

By doping a YFO nanoparticle with ions at the Y site, we observe an increase in the polarization P with increasing doping concentrations of Mn, Co and Yb; in these instances, the ionic radius is smaller than that of the Y ion, i.e., there appears to be a decreasing of the lattice parameters and a compressive strain (see Figure 5, curves 1–3). Conversely, for Sm doping, in which ionic radius is larger that that of Y, we have a tensile strain and P decreases with increasing Sm concentration (see Figure 5, curve 4). Unfortunately, there are not many experimental data for $P(x)$. Recently, Martinez et al. [30] and Gonzales [17] have determined the magnetic and ferroelectric properties of Bi^{3+}-doped YFO and observed an enhanced multiferroism. Deka et al. [46] reported an increase in the dielectric constant in Mn-doped YFO.
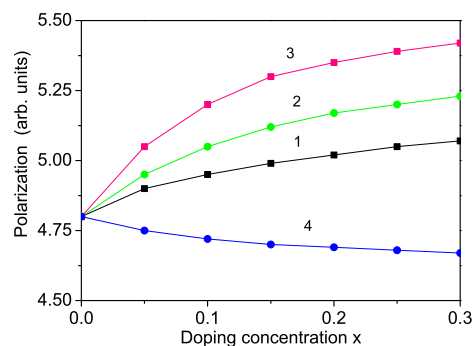

Figure 5. (Color online) The spontaneous polarization P_s as a function of the doping concentration of a (1) Mn-doped (with $J'_d = 1.5J'_b$), (2) Co-doped (with $J'_d = 1.4J'_b$), (3) Tb-doped (with $J'_d = 1.1J'_b$) and (4) Sm-doped ($J'_d = 0.6J'_b$) YFO nanoparticle for T = 300 K and N = 10 shells.

3.5. Temperature and Magnetic Field Dependence of the Phonon Energy

As a next step, we have investigated the phonon energy ω and phonon damping γ of the A_g mode ω = 149 cm^{-1} [8] in a YFO nanoparticle as a function of temperature with $R < 0$ (see Figure 6, curve 1). It can be seen that at the Neel temperature T_N, the phonon energy ω (curve 1) shows an anomaly for the case without a magnetic field, h = 0, in agreement with Ref. [8]. We obtain a decrease of the phonon mode with increasing temperatures for $R < 0$. This result is due to the strong spin-phonon interaction in YFO [8–10]. By applying an external magnetic field, h = 50 kOe, ω decreases and the anomaly disappears (Figure 6, curve 2).
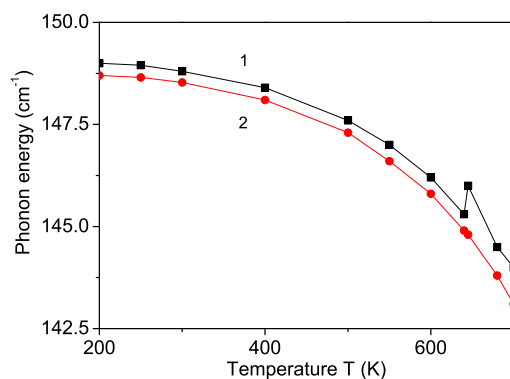

Figure 6. (Color online) Temperature dependence of the phonon mode ω = 149 cm^{-1} in a YFO nanoparticle with N = 10 shells and different magnetic fields h: 0 (1); 50 kOe (2).

3.6. Gd and Sm Doping Dependence of the Phonon Energy

We have calculated the effects of ion doping of YFO. For example, by Gd^{3+} or Sm^{3+} doping at the Y^{3+} site, the lattice parameters increase [21,24], respectively, with the increase in Gd^{3+} or Sm^{3+} content due to the resulting structure distortion, as the Gd or Sm ionic radius is slightly larger that that of Y, i.e., there is a tensile strain. This strain leads to the relation $J_d < J_b$ and, through the spin-phonon interaction, influences the phonon properties. The phonon energy decreases with increasing Gd or Sm ion concentrations, in concordance with the results reported by Bharadwaj et al. [21] and Wang et al. [24] for orthorhombic YFO.

It must be noted that Raut et al. [8] have shown that in YFO, both strong electron-phonon and strong spin-phonon coupling exist below the Neel temperature, T_N, which are also bounded together through spins. The influence of the electron-phonon interaction will be taken into account in a future paper.

3.7. Temperature and Magnetic Field Dependence of the Phonon Damping

The temperature dependence of the phonon damping γ is also calculated. γ enhances with increasing temperature (see Figure 7, curve 1) and also shows an anomaly around the Neel temperature, T_N, which disappears by applying an external magnetic field (see Figure 7, curve 2). Unfortunately, there does not appear to be published experimental data for $\omega(h)$ and $\gamma(h)$ in YFO.
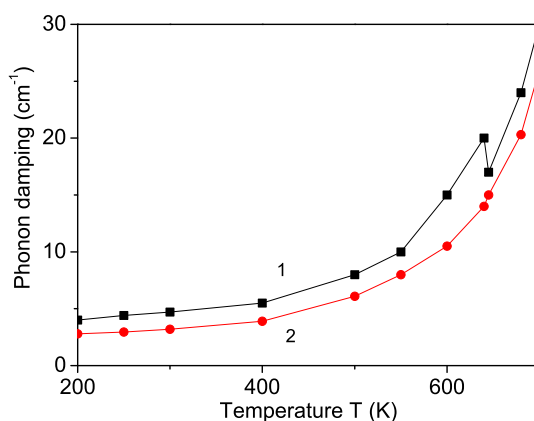

Figure 7. (Color online) Temperature dependence of the damping of the phonon mode $\omega = 149$ cm^{-1} in a YFO nanoparticle with $N = 10$ shells and different magnetic fields h: 0 (1); 50 kOe (2).

We obtain that by doping with different ions, the phonon damping increases, because it is proportional to R^2, i.e., the Raman lines are broader [24].

3.8. Ion Doping Effects on the Band Gap Energy

3.8.1. Ti Ion Doping at the Fe Site

The band gap energy E_g is observed from Equation (11) for pure and ion-doped YFO nanoparticles. We consider at first the case of a Ti^{3+}-doped YFO nanoparticle, $YFe_{1-x}Ti_xO_3$. The lattice parameters increase with increasing Ti dopants because the ionic radius of the Ti ion ($r = 0.745$ Å) is larger compared to the Fe ion ($r = 0.69$ Å). There is a tensile strain, and we use the relation $J_d < J_b$. We observe an increase in E_g (see Figure 8, curve 1).
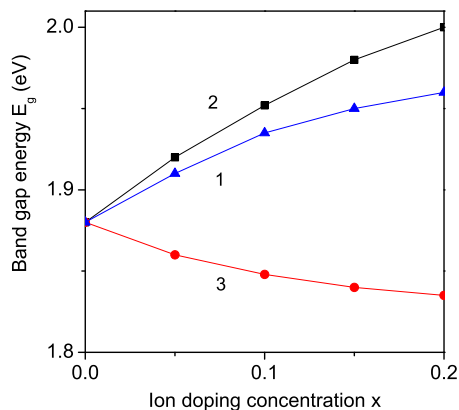
Figure 8. (Color online) Ion doping concentration dependence of the band gap energy Eg of a YFO nanoparticle (N = 10 shells) by (1) Ti doping with $J_d = 0.8J_b$; (2) Sm doping with $J_d = 0.6J_b$; (3) Co doping with $J_d = 1.4J_b$.

3.8.2. Sm Ion Doping at the Y Site

A similar enhanced E_g is also obtained by doping with Sm^{3+} ($r = 1.24$ Å) ions at the Y^{3+} ($r = 1.06$ Å), which also causes a tensile strain and enhanced band gap energy E_g (see Figure 8, curve 2), as reported by Bharadwaj et al. [21].

3.8.3. Co Ion Doping at the Fe Site

Otherwise, by Co ion doping, $YFe_{1-x}Co_xO_3$, the contrary result is observed—a reduction of the band gap energy E_g (see Figure 8, curve 3), in agreement with the results of Wang et al. [24]. This is because the ionic radius of the Co ion ($r = 0.61$ Å) is smaller than that of the Fe ion ($r = 0.69$ Å), which leads to a decrease in the lattice parameters ($J_d > J_b$) and to a decrease in the band gap energy E_g.

4. Conclusions

In conclusion, we have observed that the spontaneous magnetization M_s in a YFO nanoparticle decreases with decreasing particle size and is higher for cylindrical particles than for spherical ones. M_s is changed by ion doping, which causes different strains. Moreover, we have discussed substitution at both the Y or Fe sites. Therefore, one can obtain a material with controlled parameters. M_s increases with Co or Ni (at the Fe site) and Er (at the Y site) ion doping and decreases with Ti doping (at the Fe site). This significant enhancement in the magnetization is accompanied by a transition from antiferromagnetic to ferromagnetic behaviour, which could be used for various applications. We have tried to clarify the discrepancies of Ti-doped YFO. It must be noted that our results agree with those of Khalifa et al. [14] and Solorzano et al. [15] and disagree with the data of Madolappa et al. [16]. The phonon energy for the A_g mode $\omega = 149$ cm^{-1} and their damping decreases or increases, respectively, with increasing temperature. Both show a kink near T_N, which disappears by applying an external magnetic field. The band gap energy E_g increases with Ti or Sm ion doping and decreases with Co ion doping.

Let us emphasize that they are differences in some properties of hexagonal and orthorhombic YFO NPs which will be investigated in a future paper.

Author Contributions: Analytical calculations were performed by A.A. and J.W.; numerical calculations were performed by I.A. The results were discussed by all authors. The paper was written by J.W. All authors have read and agreed to this version of the manuscript.

Data Availability Statement: Derived data supporting the findings of this study are available from the corresponding author upon reasonable request.

Conflicts of Interest: The authors declare no conflict of interest.

References

1. Lima, E.; Martins, T.B.; Rechenberg, H.R.; Goya, G.F.; Cavelius, C.; Rapalaviciute, R.; Hao, S.; Mathur, S. Numerical simulation of magnetic interactions in polycrystalline $YFeO_3$. *J. Magn. Magn. Mater.* **2008**, *320*, 622–629. [CrossRef]
2. Shang, M.; Zhang, C.; Zhang, T.; Yuan, L.; Ge, L.; Yuan, H.; Feng, S. The multiferroic perovskite $YFeO_3$. *Appl. Phys. Lett.* **2013**, *102*, 062903. [CrossRef]
3. Jacob, K.T.; Rajitha, G.J. Nonstoichiometry, Defects and Thermodynamic Properties of $YFeO_3$, YFe_2O_4 and $Y_3Fe_5O_{12}$. *Solid State Ionics* **2012**, *224*, 32. [CrossRef]
4. Hui, S.; Xu, J.; Wu, A. Preparation and characterization of perovskite $REFeO_3$ nanocrystalline powders. *J. Rare Earths* **2010**, *28*, 416.
5. Ahmad, T.; Lone, I.H.; Ansari, S.G.; Ahmed, J.; Ahamad, T.; Alshehri, S.M. Multifunctional properties and applications of yttrium ferrite nanoparticles prepared by citrate precursor route. *Mater. Des.* **2017**, *126*, 331. [CrossRef]
6. Lone, I.H.; Ahmed, J.; Ahmad, T. Reverse Micellar Synthesis, Characterization, Magnetic and Ferroelectric Properties of $YFeO_3$ Nanoparticles. *Mater. Today Proc.* **2018**, *5*, 15303–15310. [CrossRef]
7. Nagrare, B.S.; Kekade, S.S.; Thombare, B.; Reddy, R.V.; Patil, S.I. Hyperfine interaction, Raman and magnetic study of $YFeO_3$ nanocrystals. *Solid State Commun.* **2018**, *280*, 32. [CrossRef]
8. Raut, S.; Babu, P.D.; Sharma, R.K.; Pattanayak, R.; Panigrahi, S. Grain boundary-dominated electrical conduction and anomalous optical-phonon behaviour near the Neel temperature in $YFeO_3$ ceramics. *J. Appl. Phys.* **2018**, *123*, 174101. [CrossRef]
9. Saha, J.; Jana, Y.M.; Mukherjee, G.D.; Mondal, R.; Kumar, S.; Gupta, H.C. Structure, Moessbauer spectroscopy and vibration phonon spectra in valence-bond force-field model approach for distorted perovskites $AFeO_3$ (A = La, Y). *Mater. Chem. Phys.* **2020**, *240*, 122286. [CrossRef]
10. Coutinho, P.V.; Cunha, F.; Barrozo, P. Structural, vibrational and magnetic properties of the orthoferrites $LaFeO_3$ and $YFeO_3$: A comparative study. *Solid State Commun.* **2017**, *252*, 59–63. [CrossRef]
11. Cheng, M.; Jiang, G.; Yang, W.; Duan, L.; Peng, W.; Chen, J.; Wang, X. Study of $Y_{1-x}Er_xFeO_3$ ($0 \le x \le 1$) powder synthesized by sol-gel method and their magnetic properties. *J. Magn. Magn. Mater.* **2016**, *417*, 87. [CrossRef]
12. Tien, N.A.; Diem, C.H.; Linh, N.T.T.; Mittova, V.O.; Huong, D.T.; Mittova, I.Y. Structural and magnetic properties of $YFe_{1-x}Co_xO3$ ($0.1 \le x \le 0.5$) perovskite nanomaterials synthesized by coprecipitation method. *Nanosyst. Phys. Chem. Math.* **2018**, *9*, 424–429.
13. Yuan, X.; Tang, Y.; Sun, Y.; Xu, M. Structure and magnetic properties of $Y_{1-x}Lu_xFeO_3$ ($0 \le x \le 1$) ceramics. *J. Appl. Phys.* **2012**, *111*, 053911. [CrossRef]
14. Khalifa, N.O.; Widatallah, H.M.; Gismelseed, A.M.; Al-Mabsali, F.N.; Sofin, R.G.S.; M. Pekala, M. Magnetic and Moessbauer studies of pure and Ti-doped $YFeO_3$ nanocrystalline particles prepared by mechanical milling and subsequent sintering. *Hyperfine Interact.* **2016**, *237*, 46. [CrossRef]
15. Solorzano, M.; Duran, A.; Lopez, R.; Mata, J.; Falconi, R. Magnetic and Moessbauer studies of pure and Ti-doped $YFeO_3$ nanocrystalline particles prepared by mechanical milling and subsequent sintering. *J. Mater. Sci. Mater. Electr.* **2020**, *31*, 14478–14486.
16. Madolappa, S.; Ponraj, B.; Bhimireddi, R.; Varma, K.B.R. Enhanced magnetic and dielectric properties of Ti-doped $YFeO_3$ ceramics. *J. Am. Ceram. Soc.* **2017**, *100*, 2641. [CrossRef]
17. Rosales-Gonzalez, O.; Jesus, F.S.-D.; Pedro-Garcia, F.; Cortes-Escobedo, C.A.; Ramirez-Cardona, M.; Bolarin-Miro, A.M. Enhanced Multiferroic Properties of $YFeO_3$ by Doping with Bi^{3+}. *Materials* **2019**, *12*, 2054. [CrossRef]
18. Yuan, X.; Sun, Y.; Xu, M. Effect of Gd substitution on the structure and magnetic properties of $YFeO_3$ ceramics. *J. Solid State Chem.* **2012**, *196*, 362. [CrossRef]
19. Sundarayya, Y.; Mandal, P.; Sundaresan, A; Rao, C.N.R. Moessbauer spectroscopic study of spin reorientation in Mn-substituted yttrium orthoferrite. *J. Phys. Condens. Matter* **2011**, *23*, 436001. [CrossRef]
20. Berezhnaya, M.V.; Mittova, I.Y.; Perov, N.S.; Almyasheva, O.V.; Nguyen, A.T.; Mittova, V.O; Bessalova, V.V.; Viryutina, E.L. Production of Zinc-Doped Yttrium Ferrite Nanopowders by the Sol-Gel Method. *Russ. J. Inorg. Chem.* **2018**, *63*, 742. [CrossRef]
21. Bharadwaj, P.S.J.; Kundu, S.; Kollipara, V.S.; Varma, K.B.R. Structural, optical and magnetic properties of Sm^{3+} doped yttrium orthoferrite ($YFeO_3$) obtained by sol-gel synthesis route. *J. Phys. Condens. Matter* **2020**, *32*, 035810. [CrossRef]
22. Dasari, N.; Mandal, P.; Sundaresan, A.; Vidhyadhiraja, N.S. Weak ferromagnetism and magnetization reversal in $YFe_{1-x}Cr_xO_3$. *Europhys. Lett.* **2012**, *99*, 17008. [CrossRef]
23. Ji, L.; Jiang, G.; Wu, D.; Chen, J. Study on the influence of ion doping on the crystal structure and magnetic properties of $YFeO_3$. *Mater. Res. Express* **2020**, *7*, 066103. [CrossRef]
24. Wang, M.; Wang, T. Structural, Magnetic and Optical Properties of Gd and Co Co-Doped $YFeO_3$ Nanopowders. *Materials* **2019**, *12*, 2423. [CrossRef]
25. Wang, M., Zhao, S.; Zhang, X.; Huang, C.; Zhu, Y. Effect of La addition on structural, magnetic and optical properties of multiferroic $YFeO_3$ nanopowders fabricated by low-temperature solid-state reaction method. In Proceedings of the 6th International Conference on Mechanical Engineering and Automation Science (ICMEAS), Moscow, Russia, 29–31 October 2020; Volume 1, pp. 242–246.
26. Wang, M.; Cheng, L.; Huang, L.; Pan, S.; Yao, Q.; Hu, C.; Liang, Q.; Zhou, H. Effect of Sr doped the $YFeO_3$ rare earth ortho-ferrite on structure, magnetic properties, and microwave absorption performance. *Ceram. Intern.* **2021**, in press.

27.   Treves, D. Studies on Orthoferrites at the Weizmann Institute of Science. *J. Appl. Phys.* **1965**, *36*, 1033. [CrossRef]

28.   Park, K.; Sim, H.; Leiner, J.C.; Yoshida, Y.; Jeong, J.; Yano, S.; Gardner, J.; Bourges, P.; Klicpera, M.; Sechovsky, V.; et al. Low-energy spin dynamics of orthoferrites AFeO$_3$ (A = Y, La, Bi). *J. Phys. Condens. Matter* **2018**, *30*, 235802. [CrossRef] [PubMed]

29.   Stoeffler, D.; Chaker, Z. First principles study of the electronic structure and magnetic properties of YFeO$_3$ oxide. *J. Magn. Magn. Mater.* **2017**, *442*, 255–264. [CrossRef]

30.   Martinez-Aguilar, E.; Hmok, H.L.; Ribas-Arino, J.; Beltrones, J.M.S.; Lozada-Morales, R. Structural, ferroelectric, and optical properties of Bi^{3+} doped YFeO$_3$: A first-principles study. *Int. J. Quantum Chem.* **2021**, *121*, e26551. [CrossRef]

31.   Tserkovnikov, Y.A. Decoupling of chains of Green's functions. *Teor. Mat. Fiz.* **1971**, *7*, 250. [CrossRef]

32.   Blinc, R.; Zeks, B. *Soft Modes in Ferroelectrics and Antiferroelectrics*; North-Holland: Amsterdam, The Netherlands, 1974.

33.   Pirc, R.; Blinc, R. Off-center Ti model of barium titanate. *Phys. Rev. B* **2004**, *70*, 134107. [CrossRef]

34.   Bergum, K.; Okamoto, H.; Fjellvag, H.; Grande, T.; Einarsruda, M.-A.; Selbach, S.M. Synthesis, structure and magnetic properties of nanocrystalline YMnO$_3$. *Dalton Trans.* **2011**, *40*, 7583. [CrossRef] [PubMed]

35.   Chen, P.; Grisolia, M.N.; Zhao, H.J.; Gonzalez-Vazquez, O.E.; Bellaiche, L.; Bibes, M.; Liu, B.-G.; Iniguez, J. Energetics of oxygen-octahedra rotations in perovskite oxides from first principles. *Phys. Rev. B* **2018**, *97*, 024113. [CrossRef]

36.   Wesselinowa, J.M.; Apostolov, A.T. Self-consistent theory of spin-phonon interactions in ferromagnetic semiconductors. *J. Phys. Condens. Matter* **1993**, *5*, 3555. [CrossRef]

37.   Michael, Th.; Trimper, S.; Wesselinowa, J.M. Size effects on static and dynamic properties of ferroelectric nanoparticles. *Phys. Rev. B* **2007**, *76*, 094107. [CrossRef]

38.   Shang, M.; Liu, H.; Zhang, L.; Sun, F.; Yuan, H.; Zhao, C. Multiferroicity in the YFeO$_3$ crystal. *Funct. Mater. Lett.* **2020**, *13*, 1950088. [CrossRef]

39.   Wesselniowa, J.M. Size and anisotropy effects on magnetic properties of antiferromagnetic nanoparticles. *J. Magn. Magn. Mater.* **2010**, *322*, 234. [CrossRef]

40.   Sui, Y.; Lu, F.; Liu, X.; Zhang, Y.; Sun, X.; Liu, C. A novel hexagonal YFeO$_3$ 3D nanomaterial with room temperature ferromagnetic properties prepared by self-assembling method. *Results Mater.* **2021**, *10*, 100186. [CrossRef]

41.   Popkov, V.I.; Almjasheva, O.V.; Semenova, A.S.; Kellerman, D.G.; Nevedomskiy, V.N.; Gusarov, V.V. Magnetic properties of YFeO$_3$ nanocrystals obtained by different soft-chemical methods. *J. Mater. Sci. Mater. Electron.* **2017**, *28*, 7163–7170. [CrossRef]

42.   Yuan, L.; Huang, K.; Wang, S.; Hou, C.; Wu, X.; Zou, B; Feng, S. Crystal Shape Tailoring in Perovskite Structure Rare-Earth Ferrites REFeO$_3$ (RE = La, Pr, Sm, Dy, Er, and Y) and Shape-Dependent Magnetic Properties of YFeO$_3$. *Cryst. Growth Des*. **2016**, *16*, 6522. [CrossRef]

43.   Arlt, G.; Hennings, D.; With, G.D. Dielectric properties of fine-grained barium titanate ceramics. *J. Appl. Phys.* **1985**, *58*, 1619. [CrossRef]

44.   Nguyen, T.A.; Pham, V.; Chau, D.H.; Mittova, V.O.; Mittova, I.Y.; Kopeychenko, E.I.; Nguyen, L.T.T.; Bui, V.X.; Nguyen, A.T.P. Effect of Ni substitution on phase transition, crystal structure and magnetic properties of nanostructured YFeO$_3$ perovskite. *J. Mol. Struct.* **2020**, *1215*, 128293. [CrossRef]

45.   Tien, N.A.; Mittova, I.Y.; Solodukhin, D.O.; Almyasheva, O.V.; Mittova, V.O.; Demidov, S.Y. Sol-Gel Formation and Properties of Nanocrystals of Solid Solutions Y$_{1-x}$Ca$_x$FeO$_3$. *Russ. J. Inorg. Chem.* **2014**, *59*, 40.

46.   Deka, B.; Ravi, S.; Perumal, A.; Pamu, D. Effect of Mn doping on magnetic and dielectric properties of YFeO$_3$. *Ceram. Int.* **2017**, *43*, 1323–1334. [CrossRef]

47.   Deka, B.; Ravi, S.; Perumal, A. Study of Exchange Bias in Mn-Doped YFeO$_3$ Compound. *J. Supercond. Nov. Magn.* **2016**, *29*, 2165–2170. [CrossRef]